

Title

Genome-wide association study in Collaborative Cross mice reveals a skeletal role for *Rhbd2*

Running title

GWAS in mouse bones reveals a new role for *Rhbd2*

Authors

Roei Levy^{1,2}, *Clemence Levet*³, *Keren Cohen*¹, *Matthew Freeman*³, *Richard Mott*⁴,
*Fuad Iraqi*⁵, *Yankel Gabet*¹

Affiliations

¹ Department of Anatomy and Anthropology, ² Department of Human Molecular Genetics and Biochemistry, and ⁵ Department of Clinical Microbiology and Immunology, Sackler Faculty of Medicine, Tel Aviv University, Tel Aviv 69978, Israel. ³ Dunn School of Pathology, South Parks Road, Oxford OX1 3RE, UK. ⁴ UCL Genetics Institute, University College London, Gower St., London, WC1E 6BT, UK.

Keywords Bone; Collaborative Cross; *Rhbd2*; GWAS; micro-CT

Abstract

Increased life expectancy is accompanied world-wide with increased prevalence of osteoporosis and associated skeletal fracture risk. Despite ongoing efforts in utilizing genomic data to fully map the genes responsible for bone mass, the full picture remains elusive. Here we took advantage of the phenotypic and genetic diversity innate in Collaborative Cross (CC) mice to identify new genetic variants associated with the development of bone microstructure. Using microcomputed tomography we examined key structural parameters in the femoral cortical and trabecular compartments of male and female mice from 34 CC lines.

The broad-sense heritability of these traits ranged between 50 to 60%. The cortical traits were especially sensitive to confounders, such as batch, month and season. Our GWAS approach revealed 5 loci significantly associated with 6 of the traits. We refined each locus by combining information mined from existing databases with that obtained from the known ancestry of the mice, to shortlist potential candidate genes. We found strong evidence for new candidate genes, in particular, *Rhbd2*. Using *Rhbd2* knockout mice, we confirmed its strong influence on bone microarchitecture.

This newly assigned function for *Rhbd2* can thus prove useful in deciphering the predisposing factors of osteoporosis and propose new therapeutic approaches.

Introduction

Osteoporosis is the most common bone disease in humans, affecting nearly half the US and European population over the age of 50 years. With the globally increasing life expectancy, osteoporosis and related bone fractures are becoming a pandemic health and economic concern. By 2050, the world-wide incidence of hip fractures is expected to increase by 2.5 to 6 fold (Burge et al. 2007; Dhanwal et al. 2011). Importantly, the mortality rate in the 12 months following bone fracture is as high as 20% (Center et al. 1999). Risk of fracture is determined largely by bone density and quality/strength, which are the end result of peak values achieved at skeletal maturity and subsequent age and menopause-related bone loss. Genetic factors have a major role in determining the wide range in the so-called "normal" peak bone mass. Measures of bone status are inherently complex traits, as opposed to Mendelian traits; i.e. they are controlled by the cumulative effect and interactions of numerous genetic loci and environmental factors.

Genome-wide association studies (GWAS), including a large meta-analysis, have identified more than 50 loci associated with bone mineral density (BMD) (Mizuguchi et al. 2004; Richards et al. 2008; Styrkarsdottir et al. 2008; Trikalinos et al. 2008; Estrada et al. 2012; Paternoster et al. 2010, 2013). However, many other genes that were experimentally associated with bone mass were not confirmed by GWAS in human cohorts (Jovanovich et al. 2013; Hsu and Kiel 2012; Styrkarsdottir et al. 2013). This suggests that the BMD phenotype does not capture the structural complexity of the bone; there may be other relevant bone phenotypes not yet studied in human GWAS (Hsu and Kiel 2012), which hitherto have generally relied on areal bone mineral density (aBMD) as the sole bone feature. aBMD measured by dual energy x-ray absorptiometry (DXA) is a two dimensional projection that cannot measure bone size, individual bone

compartments' shape (whether trabecular or cortical) or underlying microstructure, and thus likely conceals important features which are assumed to be controlled by unique genetic determinants. Indeed, there is a growing body of evidence that argues for distinct genetic influences of the cortical and trabecular bone and thus they should be accordingly distinguished (Paternoster et al. 2010; Estrada et al. 2012). A recent GWAS in the Collaborative Cross (CC) mice based on DXA failed to find any heritability of BMD (Iraqi et al. 2014), whereas another report based on the same mouse panel showed highly significant heritability levels in most of the cortical and trabecular microstructural parameters measured by micro-computed tomography (μ CT)(Levy et al. 2015)

Traditional peripheral quantitative CT (pQCT) has the capacity to distinguish between the cortical and trabecular bone compartments, but it lacks the required resolution to detect microstructural differences. A recent report based on high resolution pQCT (HR-pQCT) data in humans, identified two novel bone-related loci, thus far undetected by DXA and pQCT-based GWAS (Paternoster et al. 2010). Another (Karasik et al. 2016), found strong genetic correlations between 1047 adult participants of the Framingham heart study, therefore indicating that the heritability of bone microstructure constitutes a phenotypic layer which is at least partially independent of DXA-derived BMD. Like HR-pQCT studies in humans, understanding the genetic regulation of bone microstructural parameters using μ CT in small animals is likely to identify genetic factors distinct from those previously identified for DXA-derived traits.

The CC mouse panel is designed to provide high resolution analysis of complex traits, with particular emphasis on traits relevant to human health (Threadgill et al. 2002; Churchill et al. 2004). This unique resource currently consists of a growing

number of recombinant inbred lines (RIL) generated from full reciprocal breeding of eight divergent strains of mice (Collaborative Cross Consortium 2012). In contrast to commonly used laboratory mouse strains, the ancestry of the CC lines includes wild-derived inbred strains that encompass genetic variations accumulated over ~1 million years (Keane et al. 2011); more than 50 million single nucleotide polymorphisms segregate in founders of the CC. The high genetic diversity means that QTLs can be mapped using this panel that would have been invisible in a population that involved only classical strains (Roberts et al. 2007; Durrant et al. 2011b).

This claim is substantiated in a recent study that identified a genome-wide significant association between *Oxt* (oxytocin) and *Avp* (vasopressin) and skeletal microarchitecture in CC mice (Levy et al. 2015). Here, our GWAS in the CC mouse panel identified a novel gene, *Rhbd2*, associated with bone traits and using a specific knockout model we validated its role in the regulation of cortical and trabecular bone structure. This exemplifies the effectiveness and relative ease by which a GWAS with a small CC population can associate a bone-related function to novel genes, and to reveal overlooked key players in skeletal biology.

Results

CC lines widely differ in bone microarchitecture traits

We examined the variation in femoral cortical and trabecular microstructure between 34 unique CC lines totaling in 174 mice (71 females and 103 males, with an average of 4.25 mice per line). In the trabecular bone compartment we measured bone volume fraction (BV/TV), trabecular number (Tb.N), thickness (Tb.Th), connectivity (Conn.D), and spacing (or separation; Tb.Sp), as well as structural morphometric index

(SMI) of the trabecular framework. In the mid-diaphyseal cortex, we recorded cortical thickness (Ct.Th) and volumetric bone mineral density (vBMD). These traits were approximately normally distributed; BV/TV ranged from 0.017 to 0.26 (i.e. 1.7% to 26%; mean = 10.2%); Tb.N from 0.52 to 6.11 mm⁻¹ (mean = 2.7 mm⁻¹); Tb.Th from 31 to 69 μm (mean = 47 μm); Conn.D from 10.9 to 268.3 mm⁻³ (mean = 104.2 mm⁻³); SMI from 0.6 to 3.3 (mean = 2.3); Tb.Sp from 0.16 to 0.7 mm (mean = 0.33 mm); Ct.Th from 0.14 to 0.29 mm (mean = 0.2 mm); and vBMD from 402.5 to 809.2 mgHA/cm³ (mean = 581.1 mgHA/cm³). μCT images taken from two mice with distinct cortical (Fig. 1A) and trabecular (Fig. 1B) characteristics demonstrate the great variation in bone traits due solely to the genetic background. Color-codes on the graphs in Fig. 2 indicate Duncan's least significance range (LSR), which dictates whether the mean value of a line, or a group of lines, for a given trait differs to a degree of at least *P*-value < 0.001 from any other group. LSR allows for a visual representation of the heterogeneity amongst the lines. With 11 distinct groups, vBMD (Fig. 2B) is the most heterogeneous trait, while SMI and Conn.D are the least, with only 3 significantly distinct groups (Fig. 2A). Notably, the heterogeneity of females is greater than that of males for cortical traits but milder for trabecular traits (Figs. S1A1, 2 for males and S1B1, 2 for females).

To examine the inter-dependency between the traits, we assessed the correlation between all the measured parameters, in a pairwise fashion using Pearson's correlation test. The strongest correlation was between BV/TV and Tb.N (Pearson's *r* = 0.94), in line with our previous findings (Levy et al. 2015), while the weakest was between Tb.N and vBMD (*r* < 0.01). There was also a moderately high correlation between Ct.Th and

Tb.Th ($r = 0.61$; and see Table S1). The correlation between sexes for each trait (Table 1) ranged from $r = 0.75$ (Tb.Sp) to $r = 0.20$ (Ct.Th). Body weight (range = 17.4 - 35.0 gr) did not significantly correlate with any of the traits ($r = 0.01$ for Conn.D to $r = 0.19$ for Ct.Th; data not shown). After separating males from females the correlation slightly increased, yet remained low. Weak correlation was found between weight and Tb.N, SMI, and Ct.Th for females (Pearson's $r = -0.20, 0.23,$ and 0.25 respectively), and between weight and Tb.Th and Tb.Sp (Pearson's $r = 0.25$ and -0.25) for males.

While in most lines the traits' correlations were predictive of a given line's rank, in others a less expected pattern was observed; e.g., IL-1513 displayed unusually extreme phenotypes for all trabecular traits and was at the higher end for BV/TV, Tb.N, Tb.Th, and Conn.D and at the lower end for SMI and Tb.Sp, but IL-188 was more discordant between these same traits (Fig. 2 and Table S3), illustrating unexpected co-variation of the traits in the CC.

Heritability and confounder-control

We quantitated the effects of the covariates sex, age, batch, month, season, year, and experimenter on each trait. Age ranged from 9 (n=6) to 13 (n=9) weeks and the mice were dissected in 20 batches over a three-year course across 8 months during winter, spring and summer, by two experimenters. Whereas age alone had no effect on any trait, sex affected only Ct.Th; batch affected Tb.Th, vBMD, and Ct.Th; month affected Tb.Sp, vBMD, and Ct.Th; season and year affected vBMD and Ct.Th; and Tb.Th and Ct.Th were affected by experimenter. The cumulative effect of the covariates' pairwise interactions was noted for Tb.Th, SMI, vBMD, and Ct.Th. (Table S2).

We then estimated the broad-sense heritability (H^2) of each trait among the CC lines, which includes additive and non-additive epistatic effects and gene-environment interactions. The greatest H^2 is seen for Tb.N (0.63, $\log P = 13.76$; where $\log P$ stands for the negative 10-base logarithm of the P value and tests the null hypothesis that the heritability is zero), and the smallest for Ct.Th (0.51, $\log P = 7.63$).

We calculated the heritability for the mean values in each line to get a better representation of the percentage of genetic contribution to the phenotypic heterogeneity by incorporating H^2 and the average number of lines (Atamni et al. 2016). This defines H^2n , which is directly proportional to H^2 (Methods; Table 1) and ranges between 82 (Ct.Th) and 88% (Tb.N and Tb.Sp).

Overall the cortical traits seemed more prone to covariate variation; they were particularly sensitive to sex, batch, and season. This stands in contrast to our previous results (Levy et al. 2015) where BV/TV, Tb.N, and Conn.D displayed a profound sex effect, although there cortical traits were not measured. This means there is a deeper, complex layer of sex effect dependent upon cooperative environmental and genetical factors which requires further work to fully comprehend.

Association analysis for microarchitectural traits highlights 5 QTLs

We first measured statistical association between each trait and the founder haplotype at each locus in the genome. Association analyses of the cortical and trabecular traits to the haplotypes segregating in the CC (as defined by the ~70 K MegaMuga SNPs) yielded 5 distinct QTLs. For BV/TV and Tb.N we recognized a marked peak at a locus of length ~0.45 Mb between 116.5 and 116.9 Mb on chromosome 11, with peak $\log P$ values of 7.6 and 6.8, which extended above the 99th percentile permutation-threshold

by 2.7 and 1.94 logP units, respectively. In Tb.Th, Tb.Sp, Ct.Th, and vBMD we identified different QTLs on chromosomes 4, 5, 4 and 3, with logPs of 8.0, 9.4, 8.2, and 9.8, respectively, above threshold (Fig. 3 and Table 2). To account for false positive results, we kept the false discovery rate (FDR) at 1% for each scan, by employing the Benjamini–Hochberg multiple testing procedure on the logPs of the haplotype associations to the traits. Conn.D and SMI lacked significant peaks above the stringent permuted threshold and thus were not further analyzed (Fig. S2), but Conn.D displayed a borderline peak in a region that matches the peak identified for BV/TV and Tb.N. The 5 QTLs we describe are hereafter referred to as *Trl* (trabecular related locus) 7-9, and *Crl* (cortical related locus) 1-2 (respectively for BV/TV and Tb.N, Tb.Th, Tb.Sp, Ct.Th, and vBMD, and in keeping with our previous report (Levy et al. 2015) that introduced *Trl* 1-6). The 95% widths of the confidence intervals ranged from 6.4 to 15.6 Mb for the *Trls*, and were between 8.5-10.8 Mb for the *Crls* (Table 2 and Fig. S3).

We measured the contribution of each CC founder to the QTLs, relative to the wild-derived strain WSB/EiJ (Fig. 4). *Trl7* is mostly affected by the classic laboratory strains 129S1/SvImJ, NOD/LtJ, and NZO/HiLtJ; notably, the other traits were more strongly driven by the following wild strains: *Trl8* and *Crl2* by PWK/PhJ; *Trl9* by WSB/EiJ; and *Crl1* by CAST/Ei.

For *Trl7*, at the SNP most adjacent to the QTL peak UNC20471277, we found that the majority of lines with a TT allelic variant (where T refers to the nucleic acid Thymine) mostly congregate at the higher end of the BV/TV and Tb.N values (Mean BV/TV = 17%); lines with a CC variant (where C refers to the nucleic acid Cytosine) are at the lower end (mean BV/TV = 10%); and those with a CT variant are at the

intermediate range (Fig. 5). Largely, the more the trait examined is distantly correlated with BV/TV, the less differentiated the CC and TT variants are, at the SNP UNC20471277. This is accentuated in vBMD where there is a weak correlation with BV/TV (Table S1) and leveled CC and TT groups (P value = 0.8 Welch's two sample t-test).

Candidate genes identified by merge analysis and publicly available datasets

To identify the gene most likely driving the skeletal trait, we next performed a merge analysis and RNA-seq analysis and used a scoring system to rank the potential candidates.

Merge analysis uses the catalogue of variants segregating in the eight CC founders to impute the genotype dosage of each SNP in each CC line, based on the haplotype reconstruction used for haplotype association (Yalcin et al. 2005). Candidate causal variants, if they exist, would be expected to be more significant (have higher logP values) than the haplotype-based test in the flanking region. We found that *Trl7* had the highest density of polymorphisms (grey and crimson dots) with merge-logP values above the haplotype logPs (continuous black line), while *Trl8* and *Cr12* had very few. The two latter loci congregated more upstream, in accordance with the left-skewness of their respective CI simulations (Fig. S3). By calculating the relative density of merge logP values which are considerably higher than the haplotype merge logPs - and above the 99th percentile threshold for each scan - at intervals defined by each gene within the QTLs (in meaningful regions; usually between the 50th and 90th CI

percentile) we devised a gene ranking scale (Table S4). For example, while the proportion of merge analysis SNPs for BV/TV and Tb.N with logPs greater than that of the haplotype scan is 1.4% at the genome-wide scale (as well as at the region spanning the 95% CI, between ~112 – 118 Mb), it is 9.4% and ranked 5/36 (for BV/TV) or 14.07% and ranked 3/36 (for Tb.N) at the region in which the gene *Rhdbf2* is situated (~116.5 – 116.6 Mb) (See Table S4 and further discussion below).

To strengthen the criteria that classifies potential putative candidate gene as true positives, we analyzed RNA-seq datasets of osteoclasts (Fig. S4) and osteocytes (Fig. S5) made publicly available by Kim *et al* (Kim et al. 2016) (Gene Expression Omnibus accession number GSE72846) and St John *et al* (St. John et al. 2014) (Gene Expression Omnibus accession number GSE54784). We focused on local maximas that span ~0.5 Mb in and around the peaks suggested by the merge analysis, for each QTL. From the raw count reads we found that *Trl7* had the strongest gene expression differential; e.g while *Mxra7* in the osteoclasts was expressed to a negligible degree (Fig. S4A), it had a strong presence in osteocytes (Fig. S5A), whereas the genes of the other loci had much less prominent differences. This suggests that genes at *Trl7* are differentially expressed between osteocytes and osteoclasts more prominently than in the other loci.

For each of the genes with the highest merge analysis scores in *Trl7*, we attributed an *osteoclast* and *osteocyte* RNA-seq ($S_{\text{RNA-seq1}}$ and $S_{\text{RNA-seq2}}$, respectively) based on the following formula: $S_{\text{RNA-seq}} = 1 - \frac{r}{n}$, where r is the local gene rank and n is the total number of genes at the locus, where if $n > 10$ then $n = 10$. For example, *Ube2o* had an *osteoclast* RNA-seq score of 0.8 (ranked 2nd out of $n > 10$ genes) and *osteocyte* RNA-seq score of 0.8. *Rhdbf2* had an *osteoclast* RNA-seq score of 0.9 (ranked 1st) and *osteocyte* RNA-seq score of 0.7.

We then summed the cumulative *MS* (**Merge and Sequencing**) score for each gene defined as $MS = \ln(\text{merge}) + (S_{\text{RNA-seq1}} + S_{\text{RNA-seq2}})$. Our analytical approach and ranking strategy enabled us to shortlist the most plausible causal genes at the QTLs. In *Tlr7*, *Ube2o* had an $MS_{Ube2o} = 2.4 + (0.8 + 0.8) = 4.0$; while *Aanat* scored $MS_{Aanat} = 2.7 + (0 + 0) = 2.7$, and *Rhdbf2* scored $MS_{Rhdbf2} = 2.6 + (0.9 + 0.7) = 4.2$. In the other loci, the highest ranked genes were *Klf17* and *Kdm4a* for *Trl8*; *Barhl2* and *Zfp644* for *Trl9*; *Asph* and *Gdf6* for *Crl1*; and *Hfe2*, *Acp6*, *Bcl9*, and *Notch2* for *Crl2*.

Because BV/TV is a predominant parameter in bone biology, we first focused on *Trl7*. *Rhdbf2* was located near the haplotype mapping peak, and because it received the highest *MS* score, it was retained for validation. An exhaustive list of the genes under the 50, 90, and 95% CI of the QTL, is supplied in table S4.

Validation of the skeletal role of *Rhdbf2* in knock-out mice

Femora of male mice (n=14) null at *Rhdbf2* were measured for the same morphometric traits as selected for the GWAS. They were compared to their wild-type (WT) counterparts (n=13), after adjusting for batch, age and weight.

Strikingly, *Rhdbf2*^{-/-} mice had a significant bone phenotype. In line with our GWAS data, *Rhdbf2*^{-/-} mice displayed a highly significant increase in BV/TV and Tb.N (Fig. 7, 8). As expected, *Rhdbf2* KO also affected other microstructural parameters, partly due to the high correlation between the trabecular traits. After adjusting for confounders, we observed a significant difference between KO and WT animals in Tb.Sp (P value < 0.001; uncorrected P value = 0.017), SMI (P value = 0.03; uncorrected P value = 0.156) and Conn.D (P value = 0.008; uncorrected P value = 0.046). Tb.Th and vBMD were not affected by the knockout. Although the cortical compartment did

not display a haplotype peak at the vicinity of *Trl7* in the CC animals. However, after adjusting for confounders, we observed a significant difference in Ct.Th between KO and WT bones (P value = 0.01), suggesting that the role of *Rhbd2* is not limited to the trabecular compartment.

Discussion

Genetic reference population (GRP) are very efficient for the study of complex traits and biological systems, because (i) genotyping is only required once (“genotype once, phenotype many times”, see below), and (ii) replicate individuals with the same genotype can be generated at will allowing for optimal experimental designs (Broman 2005).

Here we characterize several key microstructural properties of the mouse femoral bone to assess the extent to which they are heritable; to what environmental perturbations they are prone; and to identify candidate genes by which they are controlled. By combining various statistical and high-throughput sequencing analyses together with literature data mining, we were able to shortlist putative candidate genes for 6 of the 8 examined phenotypes. We confirm one candidate gene, *Rhbd2*, using a knockout model. This article is the second to present the results of an ongoing quest to delineate the genetic determinants that govern microstructural bone traits.

Here we included two additional trabecular (SMI and Tb.Sp) and cortical (vBMD and Tb.Th) traits. While the heritability rates assessed here - determined to be over 60% for all traits - confirmed our previous findings, the degree to which sex explains the phenotypic variation was very subtle, and appeared only for the cortical traits; this discrepancy may be due to the specific cohort composition used in this study

(Table S3), which includes a sex bias due to smaller number of females than males. We found a total of five QTLs in six traits; BV/TV and Tb.N shared one QTL, and Tb.Th, Tb.Sp, vBMD, and Ct.Th yielded one each. Importantly, although bone microarchitecture factors are complex traits, our analyses highlighted no more than two loci for each trait; it is likely that analyzing a larger number of CC lines would result in the identification of further loci.

Our analyses yielded three QTLs for the trabecular traits and 2 QTLs for the cortical traits. These are referred to as *Trl7-9*, and *Cr11-2*, respectively. *Trl7* includes *Ube2o* (Ubiquitin Conjugating Enzyme E2 O), which encodes an enzyme that is an important interactant of SMAD6; *Ube2o* monoubiquitinates SMAD6, and thereby facilitates the latter to bind BMP1 receptors (Zhang et al. 2013). The signal transduction of BMP1 is in turn limited (Horiki et al. 2004; Estrada et al. 2011), and endochondral bone formation, instead of ossification, is favored. Importantly, 4 week-old SMAD6-overexpressed mice have significantly lower humeral and vertebral BV/TV ratios than their controls (Horiki et al. 2004). In close proximity to this gene is *Rhbd2* (Rhomboid 5 Homolog 2; elaborated below) which is not yet supported by peer-reviewed reports as bearing a relation to bone, but it was our overall most likely candidate based on several observations: nearness to the peak of *Trl7*; density of associated merge-logPs relative to other *Trl7* genes; local osteoclast RNA-seq peak; canonical role in secretion of TNF α (tumor necrosis factor α) and regulation of CSF1R (macrophage stimulating factor 1 receptor, a critical regulator of osteoclasts differentiation and survival (Siggs et al. 2012; Adrain et al. 2012a; McIlwain et al. 2012; Udagawa et al. 1990) ; and involvement in inflammatory arthritis (Issuree et al. 2013).

At *Trl8*, *Klf17*, *Kdm4a*, and *Dmap1* are likely putative candidate genes. Since *Klf17* (Kruppel-Like Factor 17) is part of a network that includes BMPs (Kotkamp et al. 2014) it is more likely than a nearby gene, *St3gal3* (ST3 Beta-Galactoside Alpha-2,3-Sialyltransferase 3), to affect bone traits, although the latter has a greater merge strength. *Kdm4a* (Lysine Demethylase 4A) encodes a histone demethylase that promotes the differentiation of embryonal stem cells (ESCs) to an endothelial fate (Wu et al. 2015); endothelial cells are implied in regulation of bone formation (Collin-Osdoby 1994). *Dmap1* (DNA Methyltransferase 1 Associated Protein) which encodes a DNA-methyl transferase known to regulate obesity complications, and is differentially methylated in women with polycystic ovary syndrome (Kokosar et al. 2016; Kamei et al. 2010) had the highest meaningful merge density, and it might epigenetically regulate bone formation as well. *Trl9* includes two genes of interest to bone biology: *Barhl2* and *Zfp644*. By interacting with caspase3, which is essential for ossification (Miura et al. 2004), *Barhl2* (BarH Like Homeobox 2) can inhibit β -catenin activation (Juraver-Geslin et al. 2011), and regulate the expression of chordin, a BMP signaling-detrimental protein (Larraín et al. 2000). *Zfp644* (Zinc Finger Protein 644), which encodes a transcription repressor zinc-finger protein, is upregulated in eight week-old ovariectomized mice following treatment with estradiol (Davis et al. 2008), a treatment associated with reduced bone loss (Kameda et al. 1997). Further support for the candidacy of *Barhl2* and *Zfp644* is given by the role of *Barhl2* in the development of amacrine cells (Ding et al. 2009; Mo et al. 2004) and the association of *Zfp644* with myopia (Shi et al. 2011), a condition speculated to propagate from amacrine cell signaling (Chen et al. 2006); interestingly myopia was linked to reduced postnatal bone mineral content in humans (Pohlandt 1994) and decreased expression of BMP 2 and 5 in guinea pigs (Wang et al. 2015).

The first of two cortical loci, *Crl1* contains as likely candidates the genes *Asph* and *Gdf6*. *Asph* (Aspartate Beta-Hydroxylase) encodes a protein that has a role in regulating calcium homeostasis, which may affect bone metabolism (Pruitt et al. 2014). *Gdf6* (Growth Differentiation Factor 6) is bone morphogenetic protein 13: mice with mutated *Gdf6* exhibit deformed bone formation in various skeletal sites; it is among the earliest known markers of limb joint formation (Chang et al. 1994), expressed in joints of ankle and knee. In *Gdf6* homozygous mutant mice, bones fuse at the joints early at the segmentation stage (Settle et al. 2003). For *Crl2*, we found *Hfe2*, *Bcl9*, *Notch2*, and *Prkab2* as potential candidate genes. *Hfe2* (Hemochromatosis Type 2 (Juvenile)) encodes the BMP co-receptor hemojuvelin which is expressed in skeletal muscles (Verga Falzacappa et al. 2008) and is responsible for juvenile hemochromatosis, a condition linked to sex hormones depletion and osteoporosis (Angelopoulos et al. 2006). *Bcl9* (B-Cell CLL/Lymphoma 9), the mammalian ortholog of the gene *Legless*, encodes a protein essential to the Wnt/beta-catenin signaling which is important for bone metabolism (Baron and Kneissel 2013), without which the nuclear localization of β -catenin and myocyte differentiation are compromised (Brack et al. 2009). Of note, there are mutual effects between bone and muscle, and accumulating evidence suggest many genes show pleiotropism with respect to muscle strength and bone parameters (Karasik and Kiel 2008). *Notch2* encodes a member of the notch protein family, which influence both osteoblasts and osteoclasts (Bai et al. 2008); specifically, *Notch2* is associated with the rare Hajdu-Cheney syndrome, that includes severe osteoporosis as one of its main symptoms (Regan and Long 2013; Canalis and Zanotti 2014). For this gene, we did not find any significant merge logPs included within its limits. Interestingly, *Sec22b*, an adjacent gene, had the strongest merge logP marks in this locus but no documented link to bone biology. The third-strong gene in terms of merge

values was *Prkab2* (Protein Kinase AMP-Activated Non-Catalytic Subunit Beta 2). It encodes an enzyme which is the regulatory subunit of mitogen-activated protein kinase (AMPK). AMPK widely affects bone metabolism (Jeyabalan et al. 2012).

Based on its proximity to the *Tlr7* peak (within the 50% CI), the existing literature, and its merge strength, we identified *Rhbd2* as a likely causal gene associated with BV/TV and Tb.N. We therefore analyzed the bone phenotype of *Rhbd2*^{-/-} mice, to examine its role in the modeling of the femoral cortex and trabeculae. *Rhbd2* deletion affected all the examined trabecular traits as well as Ct.Th. While the effects on BV/TV and Tb.N were in line with the haplotype mapping, the *Rhbd2* locus did not appear in any of the other traits. This however is expected, because the genetic architecture of the working cohort is such that the assumed contributing variant of *Rhbd2* is diluted and compensated, resulting in a QTL detected only for the most affected traits. Noticeably, Tb.Sp differed greatly between the *Rhbd2*^{-/-} and control mice but did not show up at the haplotype mapping; this might be due to the great diversity of the wild-type mice in Tb.Sp, and/or the need for complete knockout rather than a mere SNP to detect significant changes in Tb.Sp, and/or the SNPs giving rise to *Trl7* are functioning variants, with differential behavior affecting only BV/TV and Tb.N. A similar interpretation may be valid for the cortical phenotype of the *Rhbd2*^{-/-} mice.

Rhbd2 encodes the iRhom2 protein, a polytopic membrane protein that is a catalytically inactive member of the rhomboid intramembrane serine proteases superfamily (Lemberg and Freeman 2007). iRhom2 is necessary in macrophages for the maturation and release of the inflammatory cytokine TNF α : it acts in the trafficking of TACE, the protease that releases active TNF α from its membrane-tethered precursor

(Adrain et al. 2012b; McIlwain et al. 2012). iRhom2 is also implicated in EGF-family growth factor signaling (Siggs et al. 2014; Hosur et al. 2014a; Li et al. 2015). With a recent report of its role in trafficking of another protein, STING, it appears that iRhom2 may have a wider role in regulating membrane trafficking (Luo et al. 2016).

Further work will be needed to identify the mechanism by which iRhom2 controls bone homeostasis; a possible direction could involve a positive feedback loop that leads to differentiation of macrophages to osteoclasts by iRhom2 that stimulates the secretion of TNF α by macrophages (Kobayashi et al. 2000; Udagawa et al. 1990); hyperactivates EGFR (Yi et al. 2008; Hosur et al. 2014b); and regulates CSF1R (Hung et al. 2014; Qing et al. 2016). Although *Rhbd2* is expressed in both the osteocyte and osteoclast lineages, one cannot rule out the possibility that this gene regulates bone remodeling by virtue of its expression in non-skeletal cells.

In summary, our analyses disclose several putative genes, several of which are newly linked to a role in bone biology. A confirmation of one such gene, *Rhbd2*, provides the first conclusive evidence for its effects on bone microstructure. This finding prompts future investigations looking into the mechanism of action of *Rhbd2* and its contribution to osteoporosis in humans.

Materials and Methods

Mice

Mice aged 10 to 13 weeks (male $n = 103$; female $n = 71$), from 34 different CC lines (average of 5 mice per line) were used in this study. The mice were at inbreeding generations of 11 to 37, which correspond to 80-99.9% genetic homozygosity, respectively. The mice were bred and maintained at the small animal facility of the

Sackler Faculty of Medicine, Tel Aviv University (TAU), Israel. They were housed on hardwood chip bedding in open-top cages, with food and distilled water available *ad libitum*, in an identical controlled environment (temperature = $25 \pm 2^\circ\text{C}$; $60\% \leq$ humidity $\leq 85\%$) and a 12-hour light/dark cycle. All experiments protocols were approved by the Institutional Animal Care and Use Committee (IACUC M-13-014) at TAU, which follows the NIH/USA animal care and use protocols. The *Rhbdl2* knock out mice and their WT counterparts were bred and maintained at the University of Oxford as approved by license PPL80/2584 of the UK Home Office.

Specimen collection

Mice were intraperitoneally euthanized with cervical dislocation performed approximately one minute after breathing stops owing to 5% Isoflurane inhalation. The *Rhbdl2* knock out mice and their WT counterparts were euthanized by inhalation of a rising concentration of carbon dioxide followed by dislocation of the neck. Left femora were harvested and fixed for 24 hours in 4% paraformaldehyde solution, and then stored in 70% ethanol.

μ CT evaluation

Whole left femora from each mouse were examined as described previously (Hiram-Bab et al. 2015) by a μ CT system (μ CT 50, Scanco Medical AG, Switzerland). Briefly, scans were performed at a 10- μm resolution in all three spatial dimensions. The mineralized tissues were differentially segmented by a global thresholding procedure (Rüeggsegger et al. 1996). All morphometric parameters were determined by a direct 3D approach (Hildebrand et al. 1999). Parameters analyzed were determined in the metaphyseal trabecular bone, which included trabecular bone volume fraction (BV/TV; %), trabecular thickness (Tb.Th; μm), trabecular number (Tb.N; mm^{-1}), trabecular

connectivity density (Conn.D; mm^{-3}), trabecular structure model index (SMI), and trabecular separation (Tb.Sp; mm). Two additional parameters are characteristics of the mid-shaft diaphysis section, and include volumetric bone mineral density (vBMD; mgHA/cm^3 [mg Hydroxy-Apatite per cm^3]) and cortical thickness (Ct.Th; mm). All parameters were generated and termed according to the Guidelines for assessment of bone microstructure in rodents using micro-computed tomography (Bouxsein et al. 2010).

Genotyping

A representative male mouse from each line was initially genotyped with a high mouse diversity array (MDA), which consists of 620,000 SNPs (Durrant et al., 2011). After about two intervals of 4 generations of inbreeding, all the CC lines were regenotyped by mouse universal genotype array (MUGA, 7,500 markers) and finally with the MegaMuga (77,800 markers) SNP array to confirm their genotype status (Collaborative Cross Consortium 2012). The founder-based mosaic of each CC line was reconstructed using a hidden Markov model (HMM) in which the hidden states are the founder haplotypes and the observed states are the CC lines, to produce a probability matrix of descent from each founder. This matrix was then pruned to about 11,000 SNPs by averaging across a window of 20 consecutive markers for faster analyses and reduction of genotyping errors (Hall et al. 2012).

Statistical analyses and data acquisition

All statistical analyses were performed with the statistical software R (R core development team 2009), including the package happy.hbrem (Mott et al. 2000).

Heritability and covariate effects. Broad-sense heritability (H^2) was obtained for each trait by fitting the trait (the independent variable) to the CC line label in a linear regression model that incorporates relevant covariates (sex, age, batch, month, season, year, and experimenter). ANOVA test was used to compare a null model (in which all dependent variables are set to 0) with linear models that fit the covariates and the CC line labels to the examined trait. Practically, the difference between the residual sum of squares (RSS; $\sum_1^n (\mu_i - \hat{\mu}_i)^2$) of the covariates model and that of the CC-line labels can be seen as the net genetic contribution to the trait. Thus, this difference divided by that of the covariate model gives an estimation of the heritability. Each covariate was calculated separately, by dividing the RSS difference between the null and full model with that of the null model. Let F_0 be the model that fits the trait to the covariates; F_1 the model that fits the trait to the covariates and the CC line label; and F_{00} the null model. Then, employing ANOVA, heritability is:

$$H^2 = (RSS(F_0) - RSS(F_1)) / RSS(F_{00}).$$

Similarly, the effects for each covariate were computed separately, by fitting each in F_0 . The covariate effect is thus:

$$(RSS(F_{00}) - RSS(F_1)) / RSS(F_{00}).$$

H^2_n was derived from H^2 according to Atamni *et al* (Atamni et al. 2016).

Haplotype mapping. Each trait was fitted in a multiple linear regression model to the probability matrix of descent from each founder, including sex and age as covariates.

The expected trait value from two ancestors, termed the genetic fit, is:

$$\mu_i = \mu + \sum_{s,t} F_{Li}(s,t)(\beta_s + \beta_t) = \mu + \sum_s \sum_t F_{Li}(s,t)\beta_s$$

where μ is a normally distributed trait mean, with sex and age incorporated; $F_{Li}(s, t)$ is the probability of descent from founders s and t ; and $\beta_s + \beta_t$ is the additive effect of founders s and t . Because $\sum_s \sum_t F_{Li}(s, t) = 2$ for a diploid organism, the maximum likelihood estimates $\hat{\beta}_s$ are not independent. Thus, they are expressed here as differences from the WSB/EiJ founder effect, so that $\hat{\beta}_{WSB} = 0$. Number of members per line was weighted and integrated in the linear model. ANOVA was then used to compare this model with a null model where the founder effects are all set to 0; the resulting F -statistic yielded the significance of the genetic model vs. the null model and the negative 10-base logarithms of the P values ($\log P$) were recorded.

Permutations of the CC lines between the phenotypes were used to set significance thresholds levels. Founder effects are the estimates derived from the multiple linear regression fit above.

Regional heritability (H_r^2) was hereafter computed by ANOVA as in the broad-sense heritability computation, except that here null linear regression fit was compared with a genetic linear regression fit with the probability matrix of the founder descent at the peak QTL as the explanatory variable.

False discovery rate (FDR) was calculated using the `p.adjust` function in R, with the method "BH" (Benjamini-Hochberg (Hochberg 2016)).

Confidence intervals. Confidence intervals (CIs) were obtained both by simulations and by the quick method of Li, 2011 (Li 2011). In the simulations, we resampled the residuals of the original linear regression fit at the peak of each QTL and rescanned 100 intervals within 7-10 Mb of the original loci to find the highest $\log P$. Accordingly, following Durrant *et al.* (Durrant et al. 2011a), 1000 QTLs were simulated: if \hat{t}_i is a random permutation of the residuals of fitted genetic model at the QTL peak, and K is

a marker interval in a neighborhood of 3.5 to 5 Mb of the QTL peak L , a set of values for each trait, Z_{iK} is provided by:

$$Z_{iK} = \hat{t}_i \exp(\hat{\mu} + \sum_s X_{Kis} \hat{\beta}_s).$$

Merge analysis

In the merge analysis the eight founder strains are partitioned and merged according to the strain distribution pattern (SDP) of the alleles at the quantitative trait nucleotides (QTN) within a given QTL (formerly obtained by the initial mapping). If we denote the polymorphism as p , then $X_p = 1$ if s has allele a at p , and $X_p = 0$ otherwise (Yalcin et al. 2005). Then, at p , the probability of i to inherit alleles a and b from s and t , respectively, within L is

$$G_{pi}(a, b) = \sum_{s,t} X_p(a, s) X_p(b, t) F_{Li}(s, t).$$

This merges the founder strains by p . The expected trait value in the merged strains can now be inferred by

$$\sum_{a,b} G_{pi}(a, b) (\beta_a + \beta_b).$$

Because this is a sub-model of the QTL model, it is expected to yield higher logP values due to a reduction in the degrees of freedom. Significance was obtained by comparing the merge model with the QTL model. Individual genes were extracted from the Sanger mouse SNP repository (http://www.sanger.ac.uk/sanger/Mouse_SnpViewer).

Merge strength. We ranked the list of genes under each QTL according to the density of merge logPs associated with them: only genes that had merge logPs above the

haplotype mapping reading, and above the threshold, plus $\log P=1$ were included. We then computed the relative density according to the density of a given gene's merge $\log P$ s versus the locus' merge $\log P$ density. Let g be the region encompassed by a gene; l the region encompassed by a QTL; and mp the merge $\log P$ values above the haplotype P values plus 1. Then $g_i(mp) = 1$ if at SNP i there exists a mp and 0 otherwise. Similarly $l_j(mp) = 1$ if at SNP j there exists a mp and 0 otherwise. The merge strength (MS) is therefore:

$$MS [\%] = 100 * \frac{\sum_i g_i(mp)}{\sum_j l_j(mp)} \%$$

RNA-seq data

RNA-seq data from osteoclasts and osteocytes was obtained from gene expression omnibus (GEO) database (accession numbers GSE72846 and GSE54784) and mapped to the *mus musculus* assembly mm10 using tophat v. 2 (Trapnell et al. 2009). Read counts were then casted on the loci of interest using the R (R Core Team 2015) package GenomicAlignments and raw read counts were taken. For the osteocytes, the data of basal level day 3 was averaged.

Acknowledgments

This study was supported by Tel Aviv University starter funds and by Israel Science Foundation (ISF) grant 1822/12 to YG, by Wellcome Trust grants 085906/Z/08/Z, 075491/Z/04, and 090532/Z/09/Z to RM, core funding by Tel-Aviv University to FI, Wellcome Trust grant 101035/Z/13/Z and the Medical Research Council (programme number U105178780) to MF, and by a fellowship from the Edmond J. Safra Center for Bioinformatics at Tel-Aviv University to RL.

References

- Adrain C, Zettl M, Christova Y, Taylor N, Freeman M. 2012a. Tumor Necrosis Factor Signaling Requires iRhom2 to Promote Trafficking and Activation of TACE. *Science (80-)* **335**: 225–228.
- Adrain C, Zettl M, Christova Y, Taylor N, Freeman M, References A. 2012b. Supporting Online Material for. **225**.
- Angelopoulos NG, Goula AK, Papanikolaou G, Tolis G. 2006. Osteoporosis in HFE2 juvenile hemochromatosis. A case report and review of the literature. *Osteoporos Int* **17**: 150–5.
- Atamni HJA-T, Mott R, Soller M, Iraqi FA. 2016. High-fat-diet induced development of increased fasting glucose levels and impaired response to intraperitoneal glucose challenge in the collaborative cross mouse genetic reference population. *BMC Genet* **17**: 10.
- Bai S, Kopan R, Zou W, Hilton MJ, Ong C, Long F, Ross FP, Teitelbaum SL. 2008. NOTCH1 regulates osteoclastogenesis directly in osteoclast precursors and indirectly via osteoblast lineage cells. *J Biol Chem* **283**: 6509–18.
- Baron R, Kneissel M. 2013. WNT signaling in bone homeostasis and disease: from human mutations to treatments. *Nat Med* **19**: 179–92.
- Bouxsein ML, Boyd SK, Christiansen BA, Guldborg RE, Jepsen KJ, Müller R. 2010. Guidelines for assessment of bone microstructure in rodents using micro-computed tomography. *J Bone Miner Res* **25**: 1468–86.
- Brack AS, Murphy-Seiler F, Hanifi J, Deka J, Eyckerman S, Keller C, Aguet M, Rando TA. 2009. BCL9 is an essential component of canonical Wnt signaling that mediates the differentiation of myogenic progenitors during muscle

- regeneration. *Dev Biol* **335**: 93–105.
- Broman KW. 2005. The genomes of recombinant inbred lines. *Genetics* **169**: 1133–46.
- Burge R, Dawson-Hughes B, Solomon DH, Wong JB, King A, Tosteson A. 2007. Incidence and economic burden of osteoporosis-related fractures in the United States, 2005-2025. *J Bone Miner Res* **22**: 465–75.
- Canalis E, Zanotti S. 2014. Hajdu-Cheney syndrome: a review. *Orphanet J Rare Dis* **9**: 200.
- Center JR, Nguyen T V, Schneider D, Sambrook PN, Eisman JA. 1999. Mortality after all major types of osteoporotic fracture in men and women: an observational study. *Lancet (London, England)* **353**: 878–82.
- Chang SC, Hoang B, Thomas JT, Vukicevic S, Luyten FP, Ryba NJ, Kozak CA, Reddi AH, Moos M. 1994. Cartilage-derived morphogenetic proteins. New members of the transforming growth factor-beta superfamily predominantly expressed in long bones during human embryonic development. *J Biol Chem* **269**: 28227–34.
- Chen JC, Brown B, Schmid KL. 2006. Evaluation of inner retinal function in myopia using oscillatory potentials of the multifocal electroretinogram. *Vision Res* **46**: 4096–103.
- Churchill G a, Airey DC, Allayee H, Angel JM, Attie AD, Beatty J, Beavis WD, Belknap JK, Bennett B, Berrettini W, et al. 2004. The Collaborative Cross, a community resource for the genetic analysis of complex traits. *Nat Genet* **36**: 1133–7.
- Collaborative Cross Consortium. 2012. The genome architecture of the Collaborative

- Cross mouse genetic reference population. *Genetics* **190**: 389–401.
- Collin-Osdoby P. 1994. Role of vascular endothelial cells in bone biology. *J Cell Biochem* **55**: 304–9.
- Davis AM, Mao J, Naz B, Kohl JA, Rosenfeld CS. 2008. Comparative effects of estradiol, methyl-piperidino-pyrazole, raloxifene, and ICI 182 780 on gene expression in the murine uterus. *J Mol Endocrinol* **41**: 205–17.
- Dhanwal DK, Dennison EM, Harvey NC, Cooper C. 2011. Epidemiology of hip fracture: Worldwide geographic variation. *Indian J Orthop* **45**: 15–22.
- Ding Q, Chen H, Xie X, Libby RT, Tian N, Gan L. 2009. BARHL2 differentially regulates the development of retinal amacrine and ganglion neurons. *J Neurosci* **29**: 3992–4003.
- Durrant C, Tayem H, Yalcin B, Cleak J, Goodstadt L, de Villena FP-M, Mott R, Iraqi F a. 2011a. Collaborative Cross mice and their power to map host susceptibility to *Aspergillus fumigatus* infection. *Genome Res* **21**: 1239–48.
- Durrant C, Tayem H, Yalcin B, Cleak J, Goodstadt L, Villena FP De, Mott R, Iraqi FA. 2011b. Collaborative Cross mice and their power to map host susceptibility to *Aspergillus fumigatus* infection Collaborative Cross mice and their power to map host susceptibility to *Aspergillus fumigatus* infection.
- Estrada K, Styrkarsdottir U, Evangelou E, Hsu Y-H, Duncan EL, Ntzani EE, Oei L, Albagha OME, Amin N, Kemp JP, et al. 2012. Genome-wide meta-analysis identifies 56 bone mineral density loci and reveals 14 loci associated with risk of fracture. *Nat Genet* **44**: 491–501.
- Estrada KD, Retting KN, Chin AM, Lyons KM. 2011. Smad6 is essential to limit BMP signaling during cartilage development. *J Bone Miner Res* **26**: 2498–510.

- Hall M, Manship G, Morahan G, Pettit K, Scholten J, Tweedie K, Wallace A, Weerasekera L, Aylor DL, Baric RS, et al. 2012. The genome architecture of the Collaborative Cross mouse genetic reference population. *Genetics* **190**: 389–401.
- Hildebrand T, Laib A, Müller R, Dequeker J, Rügsegger P. 1999. Direct three-dimensional morphometric analysis of human cancellous bone: microstructural data from spine, femur, iliac crest, and calcaneus. *J Bone Miner Res* **14**: 1167–74.
- Hiram-Bab S, Liron T, Deshet-Unger N, Mittelman M, Gassmann M, Rauner M, Franke K, Wielockx B, Neumann D, Gabet Y. 2015. Erythropoietin directly stimulates osteoclast precursors and induces bone loss. *FASEB J* **29**: 1890–900.
- Hochberg Y. 2016. Controlling the False Discovery Rate : A Practical and Powerful Approach to Multiple Testing Author (s): Yoav Benjamini and Yosef Hochberg Source : Journal of the Royal Statistical Society . Series B (Methodological), Vol . 57 , No . 1 (1995), Publi. **57**: 289–300.
- Horiki M, Imamura T, Okamoto M, Hayashi M, Murai J, Myoui A, Ochi T, Miyazono K, Yoshikawa H, Tsumaki N. 2004. Smad6/Smurf1 overexpression in cartilage delays chondrocyte hypertrophy and causes dwarfism with osteopenia. *J Cell Biol* **165**: 433–45.
- Hosur V, Johnson KR, Burzenski LM, Stearns TM, Maser RS, Shultz LD. 2014a. Rbdf2 mutations increase its protein stability and drive EGFR hyperactivation through enhanced secretion of amphiregulin. *Proc Natl Acad Sci* **111**: E2200–E2209.
- Hosur V, Johnson KR, Burzenski LM, Stearns TM, Maser RS, Shultz LD. 2014b. Rbdf2 mutations increase its protein stability and drive EGFR hyperactivation

- through enhanced secretion of amphiregulin. *Proc Natl Acad Sci* **111**: E2200–E2209.
- Hsu Y-H, Kiel DP. 2012. Clinical review: Genome-wide association studies of skeletal phenotypes: what we have learned and where we are headed. *J Clin Endocrinol Metab* **97**: E1958-77.
- Hung JY, Horn D, Woodruff K, Prihoda T, LeSaux C, Peters J, Tio F, Abboud-Werner SL. 2014. Colony-stimulating factor 1 potentiates lung cancer bone metastasis. *Lab Invest* **94**: 371–381.
- Iraqi F a, Athamni H, Dorman A, Salymah Y, Tomlinson I, Nashif A, Shusterman A, Weiss E, Houry-Haddad Y, Mott R, et al. 2014. Heritability and coefficient of genetic variation analyses of phenotypic traits provide strong basis for high-resolution QTL mapping in the Collaborative Cross mouse genetic reference population. *Mamm Genome* **25**: 109–19.
- Issuree PDA, Marezky T, McIlwain DR, Monette S, Qing X, Lang PA, Swendeman SL, Park-Min K-H, Binder N, Kalliolias GD, et al. 2013. iRHOM2 is a critical pathogenic mediator of inflammatory arthritis. *J Clin Invest* **123**: 928–32.
- Jeyabalan J, Shah M, Viollet B, Chenu C. 2012. AMP-activated protein kinase pathway and bone metabolism. *J Endocrinol* **212**: 277–90.
- Jovanovich A, Bůzková P, Chonchol M, Robbins J, Fink HA, de Boer IH, Kestenbaum B, Katz R, Carbone L, Lee J, et al. 2013. Fibroblast growth factor 23, bone mineral density, and risk of hip fracture among older adults: the cardiovascular health study. *J Clin Endocrinol Metab* **98**: 3323–31.
- Juraver-Geslin HA, Ausseil JJ, Wassef M, Durand BC. 2011. Barhl2 limits growth of the diencephalic primordium through Caspase3 inhibition of beta-catenin

activation. *Proc Natl Acad Sci U S A* **108**: 2288–93.

- Kameda T, Mano H, Yuasa T, Mori Y, Miyazawa K, Shiokawa M, Nakamaru Y, Hiroi E, Hiura K, Kameda A, et al. 1997. Estrogen inhibits bone resorption by directly inducing apoptosis of the bone-resorbing osteoclasts. *J Exp Med* **186**: 489–95.
- Kamei Y, Suganami T, Ehara T, Kanai S, Hayashi K, Yamamoto Y, Miura S, Ezaki O, Okano M, Ogawa Y. 2010. Increased expression of DNA methyltransferase 3a in obese adipose tissue: studies with transgenic mice. *Obesity (Silver Spring)* **18**: 314–21.
- Karasik D, Demissie S, Zhou Y, Lu D, Broe KE, Bouxsein ML, Cupples LA, Kiel DP. 2016. Heritability and Genetic Correlations for Bone Microarchitecture: The Framingham Study Families. *J Bone Miner Res*.
- Karasik D, Kiel DP. 2008. Genetics of the musculoskeletal system: a pleiotropic approach. *J Bone Miner Res* **23**: 788–802.
- Keane TM, Goodstadt L, Danecek P, White M a, Wong K, Yalcin B, Heger A, Agam A, Slater G, Goodson M, et al. 2011. Mouse genomic variation and its effect on phenotypes and gene regulation. *Nature* **477**: 289–94.
- Kim K, Punj V, Kim J-M, Lee S, Ulmer TS, Lu W, Rice JC, An W. 2016. MMP-9 facilitates selective proteolysis of the histone H3 tail at genes necessary for proficient osteoclastogenesis. *Genes Dev* **30**: 208–19.
- Kobayashi K, Takahashi N, Jimi E, Udagawa N, Takami M, Kotake S, Nakagawa N, Kinoshita M, Yamaguchi K, Shima N, et al. 2000. Tumor necrosis factor alpha stimulates osteoclast differentiation by a mechanism independent of the ODF/RANKL-RANK interaction. *J Exp Med* **191**: 275–86.

- Kokosar M, Benrick A, Perfilyev A, Fornes R, Nilsson E, Maliqueo M, Behre CJ, Sazonova A, Ohlsson C, Ling C, et al. 2016. Epigenetic and Transcriptional Alterations in Human Adipose Tissue of Polycystic Ovary Syndrome. *Sci Rep* **6**: 22883.
- Kotkamp K, Mössner R, Allen A, Onichtchouk D, Driever W. 2014. A Pou5f1/Oct4 dependent Klf2a, Klf2b, and Klf17 regulatory sub-network contributes to EVL and ectoderm development during zebrafish embryogenesis. *Dev Biol* **385**: 433–47.
- Larraín J, Bachiller D, Lu B, Agius E, Piccolo S, De Robertis EM. 2000. BMP-binding modules in chordin: a model for signalling regulation in the extracellular space. *Development* **127**: 821–30.
- Lemberg MK, Freeman M. 2007. Functional and evolutionary implications of enhanced genomic analysis of rhomboid intramembrane proteases. *Genome Res* **17**: 1634–1646.
- Levy R, Mott RF, Iraqi FA, Gabet Y. 2015. Collaborative cross mice in a genetic association study reveal new candidate genes for bone microarchitecture. *BMC Genomics* **16**: 1013.
- Li H. 2011. A quick method to calculate QTL confidence interval. *J Genet* **90**: 355–60.
- Li X, Maretzky T, Weskamp G, Monette S, Qing X, Issuree PDA, Crawford HC, McIlwain DR, Mak TW, Salmon JE, et al. 2015. iRhoms 1 and 2 are essential upstream regulators of ADAM17-dependent EGFR signaling. *Proc Natl Acad Sci U S A* **112**: 6080–5.
- Luo W-W, Li S, Li C, Lian H, Yang Q, Zhong B, Shu H-B. 2016. iRhom2 is essential

for innate immunity to DNA viruses by mediating trafficking and stability of the adaptor STING. *Nat Immunol* **17**: 1057–1066.

McIlwain DR, Lang PA, Maretzky T, Hamada K, Ohishi K, Maney SK, Berger T, Murthy A, Duncan G, Xu HC, et al. 2012. iRhom2 Regulation of TACE Controls TNF-Mediated Protection Against Listeria and Responses to LPS. *Science (80-)* **335**: 229–232.

Miura M, Chen X-D, Allen MR, Bi Y, Gronthos S, Seo B-M, Lakhani S, Flavell RA, Feng X-H, Robey PG, et al. 2004. A crucial role of caspase-3 in osteogenic differentiation of bone marrow stromal stem cells. *J Clin Invest* **114**: 1704–13.

Mizuguchi T, Furuta I, Watanabe Y, Tsukamoto K, Tomita H, Tsujihata M, Ohta T, Kishino T, Matsumoto N, Minakami H, et al. 2004. LRP5, low-density-lipoprotein-receptor-related protein 5, is a determinant for bone mineral density. *J Hum Genet* **49**: 80–6.

Mo Z, Li S, Yang X, Xiang M. 2004. Role of the Barhl2 homeobox gene in the specification of glycinergic amacrine cells. *Development* **131**: 1607–18.

Mott R, Talbot CJ, Turri MG, Collins a C, Flint J. 2000. A method for fine mapping quantitative trait loci in outbred animal stocks. *Proc Natl Acad Sci U S A* **97**: 12649–54.

Paternoster L, Lorentzon M, Lehtimäki T, Eriksson J, Kähönen M, Raitakari O, Laaksonen M, Sievänen H, Viikari J, Lyytikäinen L-P, et al. 2013. Genetic determinants of trabecular and cortical volumetric bone mineral densities and bone microstructure. *PLoS Genet* **9**: e1003247.

Paternoster L, Lorentzon M, Vandenput L, Karlsson MK, Ljunggren O, Kindmark A, Mellstrom D, Kemp JP, Jarett CE, Holly JMP, et al. 2010. Genome-wide

- association meta-analysis of cortical bone mineral density unravels allelic heterogeneity at the RANKL locus and potential pleiotropic effects on bone. *PLoS Genet* **6**: e1001217.
- Pohlandt F. 1994. Hypothesis: myopia of prematurity is caused by postnatal bone mineral deficiency. *Eur J Pediatr* **153**: 234–6.
- Pruitt KD, Brown GR, Hiatt SM, Thibaud-Nissen F, Astashyn A, Ermolaeva O, Farrell CM, Hart J, Landrum MJ, McGarvey KM, et al. 2014. RefSeq: an update on mammalian reference sequences. *Nucleic Acids Res* **42**: D756-63.
- Qing X, D. Rogers L, Mortha A, Lavin Y, Redecha P, Issuree PD, Maretzky T, Merad M, R. McIlwain D, Mak TW, et al. 2016. iRhom2 regulates CSF1R cell surface expression and non-steady state myeloipoiesis in mice. *Eur J Immunol* **46**: 2737–2748.
- Regan J, Long F. 2013. Notch signaling and bone remodeling. *Curr Osteoporos Rep* **11**: 126–9.
- Richards JB, Rivadeneira F, Inouye M, Pastinen TM, Soranzo N, Wilson SG, Andrew T, Falchi M, Gwilliam R, Ahmadi KR, et al. 2008. Bone mineral density, osteoporosis, and osteoporotic fractures: a genome-wide association study. *Lancet* **371**: 1505–12.
- Roberts A, Pardo-Manuel de Villena F, Wang W, McMillan L, Threadgill DW. 2007. The polymorphism architecture of mouse genetic resources elucidated using genome-wide resequencing data: implications for QTL discovery and systems genetics. *Mamm Genome* **18**: 473–81.
- Rüegsegger P, Koller B, Müller R. 1996. A microtomographic system for the nondestructive evaluation of bone architecture. *Calcif Tissue Int* **58**: 24–29.

- Settle SH, Rountree RB, Sinha A, Thacker A, Higgins K, Kingsley DM. 2003. Multiple joint and skeletal patterning defects caused by single and double mutations in the mouse *Gdf6* and *Gdf5* genes. *Dev Biol* **254**: 116–30.
- Shi Y, Li Y, Zhang D, Zhang H, Li Y, Lu F, Liu X, He F, Gong B, Cai L, et al. 2011. Exome sequencing identifies ZNF644 mutations in high myopia. *PLoS Genet* **7**: e1002084.
- Siggs OM, Grieve A, Xu H, Bambrough P, Christova Y, Freeman M. 2014. Genetic interaction implicates *iRhom2* in the regulation of EGF receptor signalling in mice. *Biol Open* **3**.
- Siggs OM, Xiao N, Wang Y, Shi H, Tomisato W, Li X, Xia Y, Beutler B. 2012. *iRhom2* is required for the secretion of mouse TNF α . *Blood* **119**: 5769–71.
- St. John HC, Bishop KA, Meyer MB, Benkusky NA, Leng N, Kendziorski C, Bonewald LF, Pike JW. 2014. The Osteoblast to Osteocyte Transition: Epigenetic Changes and Response to the Vitamin D₃ Hormone. *Mol Endocrinol* **28**: 1150–1165.
- Styrkarsdottir U, Halldorsson B V, Gretarsdottir S, Gudbjartsson DF, Walters GB, Ingvarsson T, Jonsdottir T, Saemundsdottir J, Center JR, Nguyen T V, et al. 2008. Multiple genetic loci for bone mineral density and fractures. *N Engl J Med* **358**: 2355–65.
- Styrkarsdottir U, Thorleifsson G, Sulem P, Gudbjartsson DF, Sigurdsson A, Jonasdottir A, Jonasdottir A, Oddsson A, Helgason A, Magnusson OT, et al. 2013. Nonsense mutation in the *LGR4* gene is associated with several human diseases and other traits. *Nature* **497**: 517–20.
- Threadgill DW, Hunter KW, Williams RW. 2002. Genetic dissection of complex and

- quantitative traits: from fantasy to reality via a community effort. *Mamm Genome* **13**: 175–8.
- Trapnell C, Pachter L, Salzberg SL. 2009. TopHat: discovering splice junctions with RNA-Seq. *Bioinformatics* **25**: 1105–11.
- Trikalinos TA, Salanti G, Zintzaras E, Ioannidis JPA. 2008. Meta-analysis methods. *Adv Genet* **60**: 311–34.
- Udagawa N, Takahashi N, Akatsu T, Tanaka H, Sasaki T, Nishihara T, Koga T, Martin TJ, Suda T. 1990. Origin of osteoclasts: mature monocytes and macrophages are capable of differentiating into osteoclasts under a suitable microenvironment prepared by bone marrow-derived stromal cells. *Proc Natl Acad Sci U S A* **87**: 7260–4.
- Verga Falzacappa MV, Casanovas G, Hentze MW, Muckenthaler MU. 2008. A bone morphogenetic protein (BMP)-responsive element in the hepcidin promoter controls HFE2-mediated hepatic hepcidin expression and its response to IL-6 in cultured cells. *J Mol Med (Berl)* **86**: 531–40.
- Wang Q, Xue M-L, Zhao G-Q, Liu M-G, Ma Y-N, Ma Y. 2015. Form-deprivation myopia induces decreased expression of bone morphogenetic protein-2, 5 in guinea pig sclera. *Int J Ophthalmol* **8**: 39–45.
- Wu L, Wary KK, Revskoy S, Gao X, Tsang K, Komarova YA, Rehman J, Malik AB. 2015. Histone Demethylases KDM4A and KDM4C Regulate Differentiation of Embryonic Stem Cells to Endothelial Cells. *Stem cell reports* **5**: 10–21.
- Yalcin B, Flint J, Mott R. 2005. Using progenitor strain information to identify quantitative trait nucleotides in outbred mice. *Genetics* **171**: 673–81.
- Yi T, Lee H-L, Cha J-H, Ko S-I, Kim H-J, Shin H-I, Woo K-M, Ryoo H-M, Kim G-S,

Baek J-H. 2008. Epidermal growth factor receptor regulates osteoclast differentiation and survival through cross-talking with RANK signaling. *J Cell Physiol* **217**: 409–422.

Zhang X, Zhang J, Bauer A, Zhang L, Selinger DW, Lu CX, Ten Dijke P. 2013. Fine-tuning BMP7 signalling in adipogenesis by UBE2O/E2-230K-mediated monoubiquitination of SMAD6. *EMBO J* **32**: 996–1007.

Tables

Table 1 Heritability, sex correlations, and covariate interactions for trabecular and cortical traits

Trait	H ²	logP	H ² n	Sex Cor.	Interactions %
BV/TV	0.61	12.43	0.87	0.6695754	-
Tb.N	0.63	13.76	0.88	0.7628464	-
Tb.Th	0.54	9.08	0.83	0.7039887	34.70
Conn.D	0.56	9.90	0.84	0.5188039	-
SMI	0.55	9.43	0.84	0.2984166	26.02
Tb.Sp	0.63	13.45	0.88	0.754563	-
vBMD	0.62	12.15	0.87	0.6268818	53.92
Ct.Th	0.51	7.63	0.82	0.2055684	41.07

H² is the broad-sense heritability (which includes epistatic and environmental influences); logP is the negative 10-base logarithm of the P-value; H²n is the line-mean heritability; Sex Cor. Is the sex correlation of each trait; and interactions % refers to the relative contribution of the cumulative covariate-interactions, which include sex, age, batch, month, season, year, and experimenter (see table S2).

Table 2 Positions of QTLs associated with trabecular and cortical traits

QTL	Trait	Chr	logP	99th % thresh	H ² _r	Simulation					
						50% CI (Mb)		90% CI (Mb)		95% CI (Mb)	
						Position	Width	Position	Width	Position	Width
<i>Trl7</i>	BV/TV	11	7.60	4.90	0.69	116.6-116.7	0.12	113.6-118.1	4.50	112.1-118.3	6.40

<i>Trl7</i>	Tb.N	11	6.80	4.84	0.71	116.6- 116.87	0.29	114.2- 118.35	4.15	112.41 - 118.68	6.27
<i>Trl8</i>	Tb.Th	4	8.00	4.50	0.61	117.2- 117.58	0.32	113.05 - 125.54	12.49	110.87 - 126.52	15.65
<i>Trl9</i>	Tb.Sp	5	9.40	6.01	0.78	105.78 - 106.14	0.35	101.6- 109.11	7.54	99.8- 110.39	10.62
<i>Crl1</i>	Ct.Th	4	8.20	4.80	0.80	9.29- 9.72	0.43	4.0- 11.7	7.70	3.4 -11.8	8.49
<i>Crl2</i>	vBMD	3	9.80	4.93	0.86	97.2- 97.4	0.20	94.4- 103.1	8.50	93.22- 104.3	10.80

Chr = chromosome; logP = negative 10-base logarithm of P value; Sig = genome-wide significance level; 99th % threshold logP = threshold used to define cut-off for QTL peaks (Fig. 4); H^2_r = regional heritability (the proportion to which the locus explains the phenotypic variability). Positions and widths of the simulation-based 50, 90, and 95% CIs are given.

Figure legends

Figure 1. μ CT images of trabecular and cortical bone of the femora of representative male CC mice. **(A)** Trabecular bone. Left: IL-2452, Right: IL-1513. **(B)** Cortical bone. Left: IL-785, Right: IL-2689.

Figure 2 Trabecular and cortical traits distributions across the CC lines. X-axis is the lines, y-axis is the trait means **A.** From top left, counter-clockwise: BV/TV (%), Tb.N (mm^{-1}), Tb.Th (μm), Conn.D (mm^{-3}), SMI, and Tb.Sp (mm). **B.** Left, vBMD (mgHA/cm^3), right, Ct.Th (mm). Color codes group line(s) which significantly differ

from other groups. Lines are ordered inconsistently among the traits, per trait-specific descending order. Refer to Table S3 for more details.

Figure 3 Haplotype association maps for the trabecular and cortical traits. X-axis is the position on the chromosome, y-axis is the $-\log P$ value of the association. Lower threshold represents the 95th percentile of 200 simulations, and top represents the 99th percentile. Loci above the 99% cut-off were further investigated. From top to bottom: BV/TV, Tb.N, Tb.Th, Tb.Sp, vBMD, and Ct.Th.

Figure 4. Ancestral effects relative to WSB. Y axis is the strain deviation relative to WSB, x axis is the different strains of the eight CC founders. (A) to (F): *Trl7* to *Trl9*, *Crl1*, and *Crl2*, respectively.

Figure 5 Traits distribution at the marker UNC20471277 across bearers of homozygous and heterozygous alleles, separated by sex. X-axis is the allelic variation at the marker, y-axis is the trait value.

Figure 6 Merge analysis. Readings below $\log P = 4$ are elided for brevity. X axis is the position on the genome in Mb; y left axis is the $\log P$ score; y right axis is the recombination rate scale; colored bars are genes (note that only strong putative candidate genes are shown.); cyan line is the recombination rate; black continuous line is the haplotype test's peak; dashed line is the 99% permutation threshold. (A) to (F):

Trl7 of BV/TV, Trl7 of Tb.N, Trl8 of Tb.Th, Trl9 of Tb.Sp, Crl1 of Ct.Th, and Crl2 of vBMD, respectively.

Figure 7 *Rhbd2* knockout versus wildtype for each of the studied traits. Left is KO, right is WT. PV is the confounder-adjusted P value. The unadjusted P value is in brackets. PV = 0 means PV < 0.001.

Figure 8 μ CT images of three-dimensional representative cortical and trabecular bones reconstructions for *Rhbd2* knockout and wildtype. Left: KO, right: WT. **(A)** Trabecular bone. **(B)** Cortical bone. All samples were of male mice, aged 11 weeks.

Figures

Figure 1

Levy_Fig1

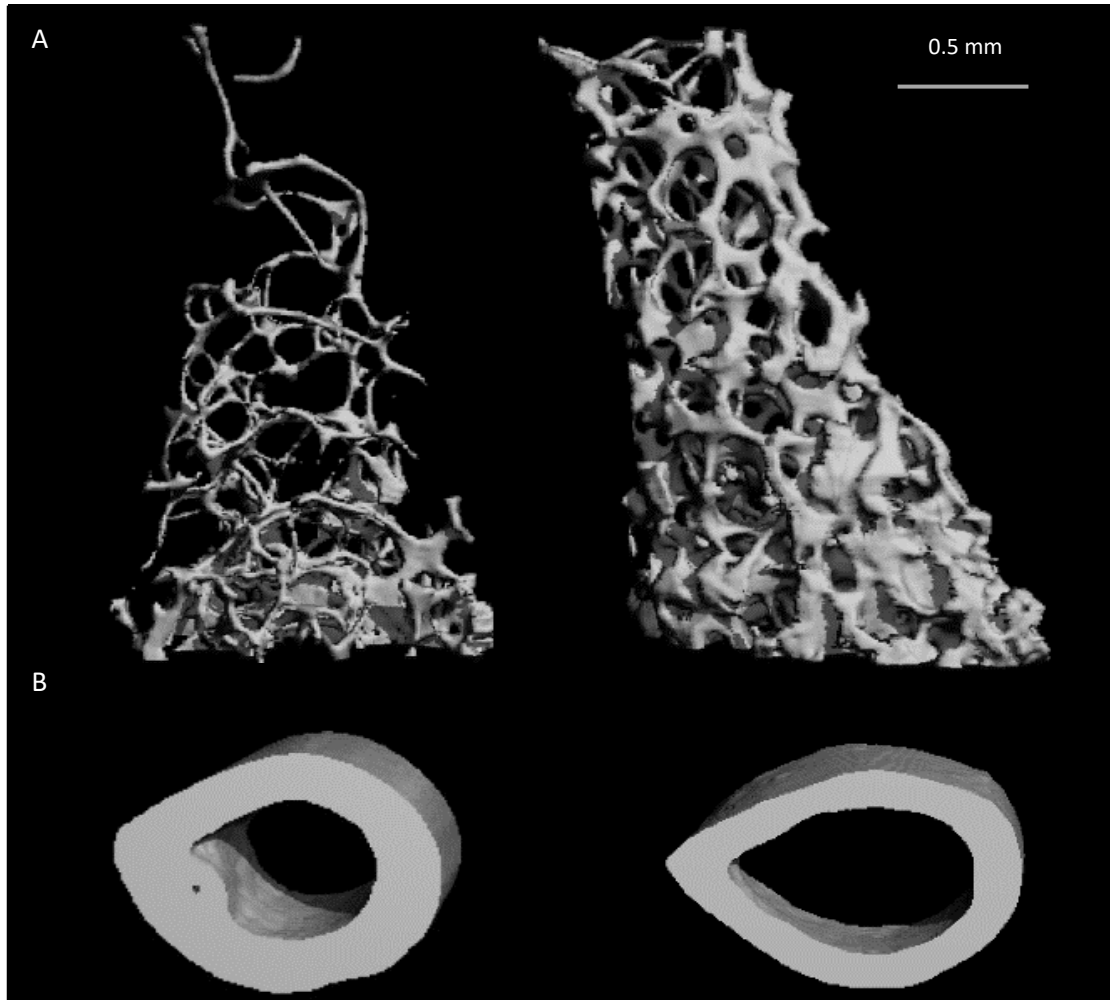


Figure 2

Levy_Fig2

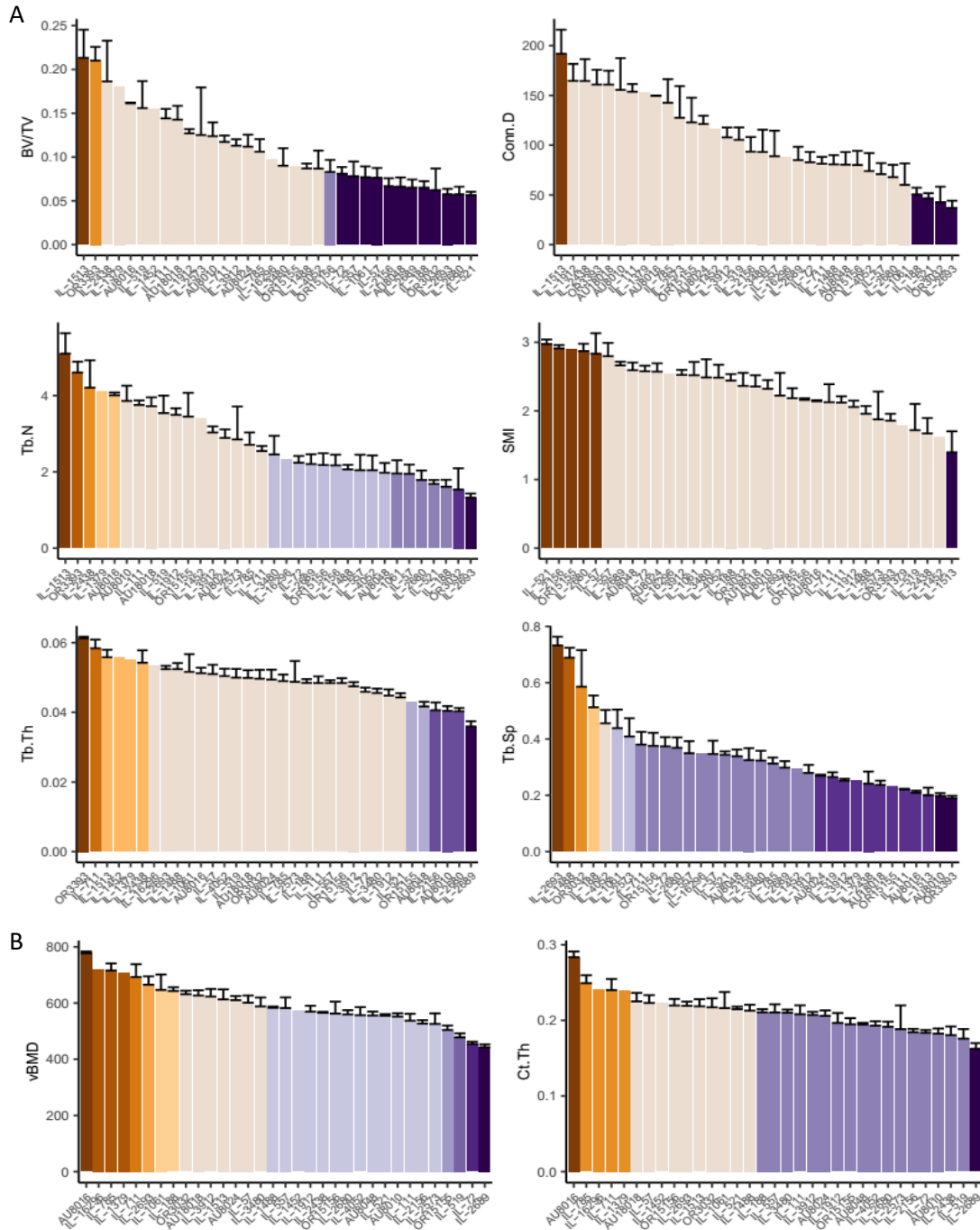


Figure 3

Levy_Fig3

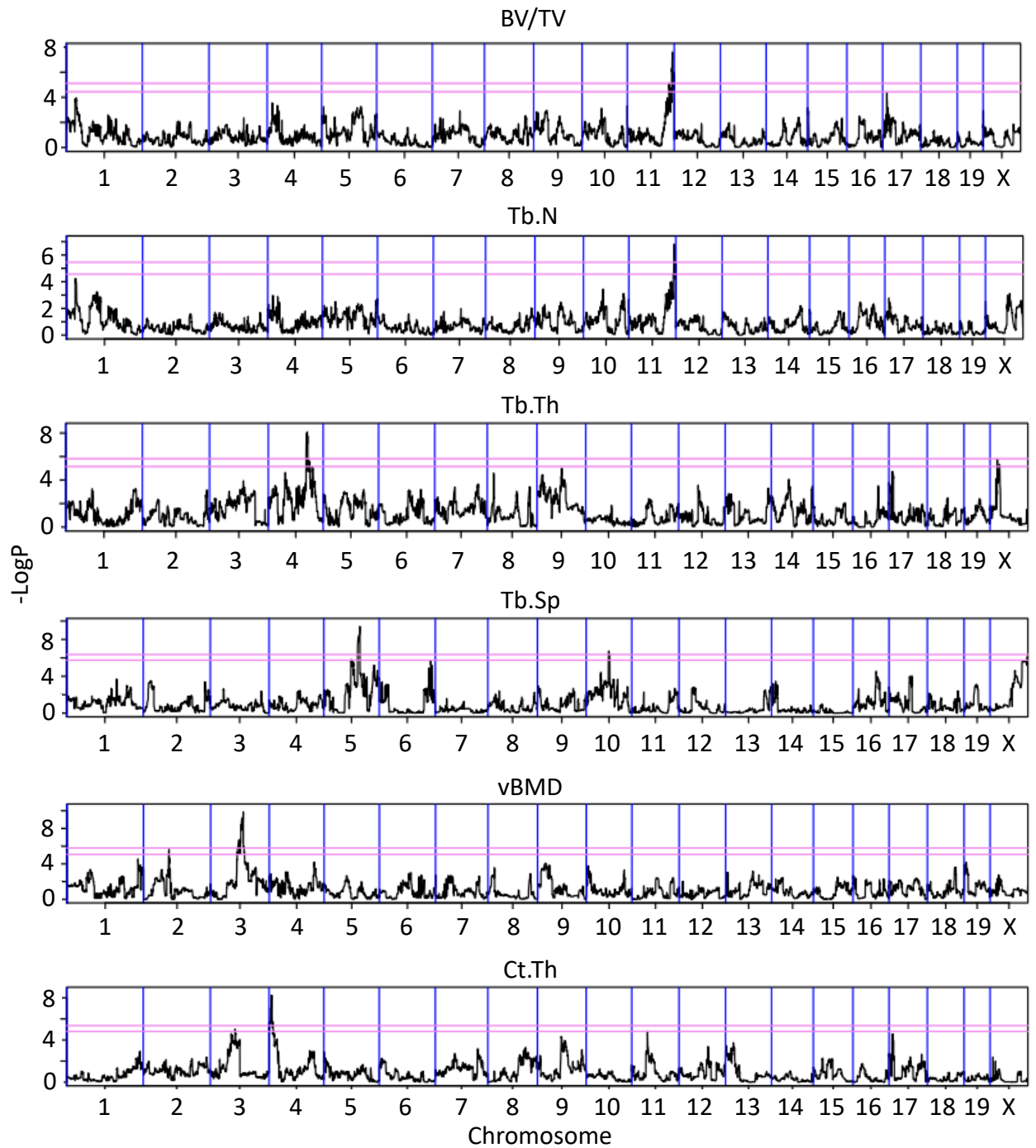


Figure 4

Levy_Fig4

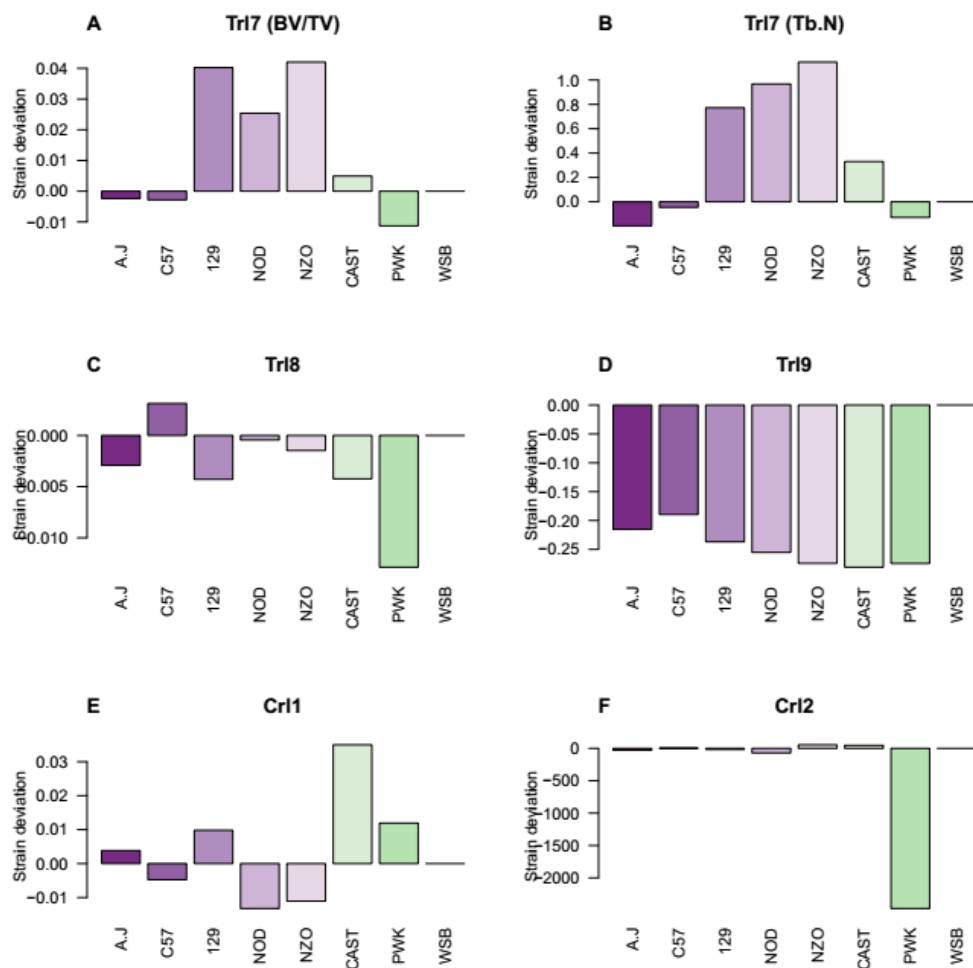


Figure 5

Levy_Fig5

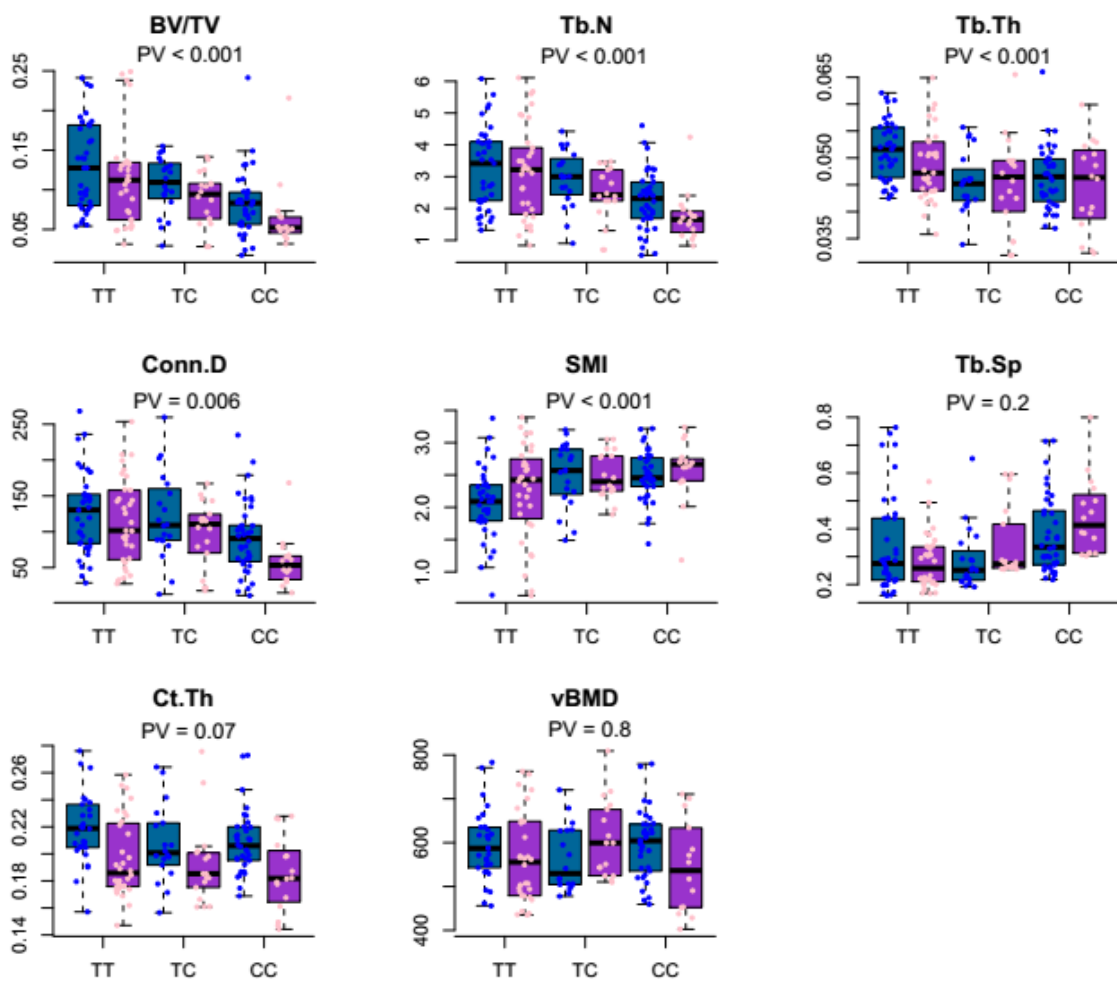


Figure 6

Levy_Fig6

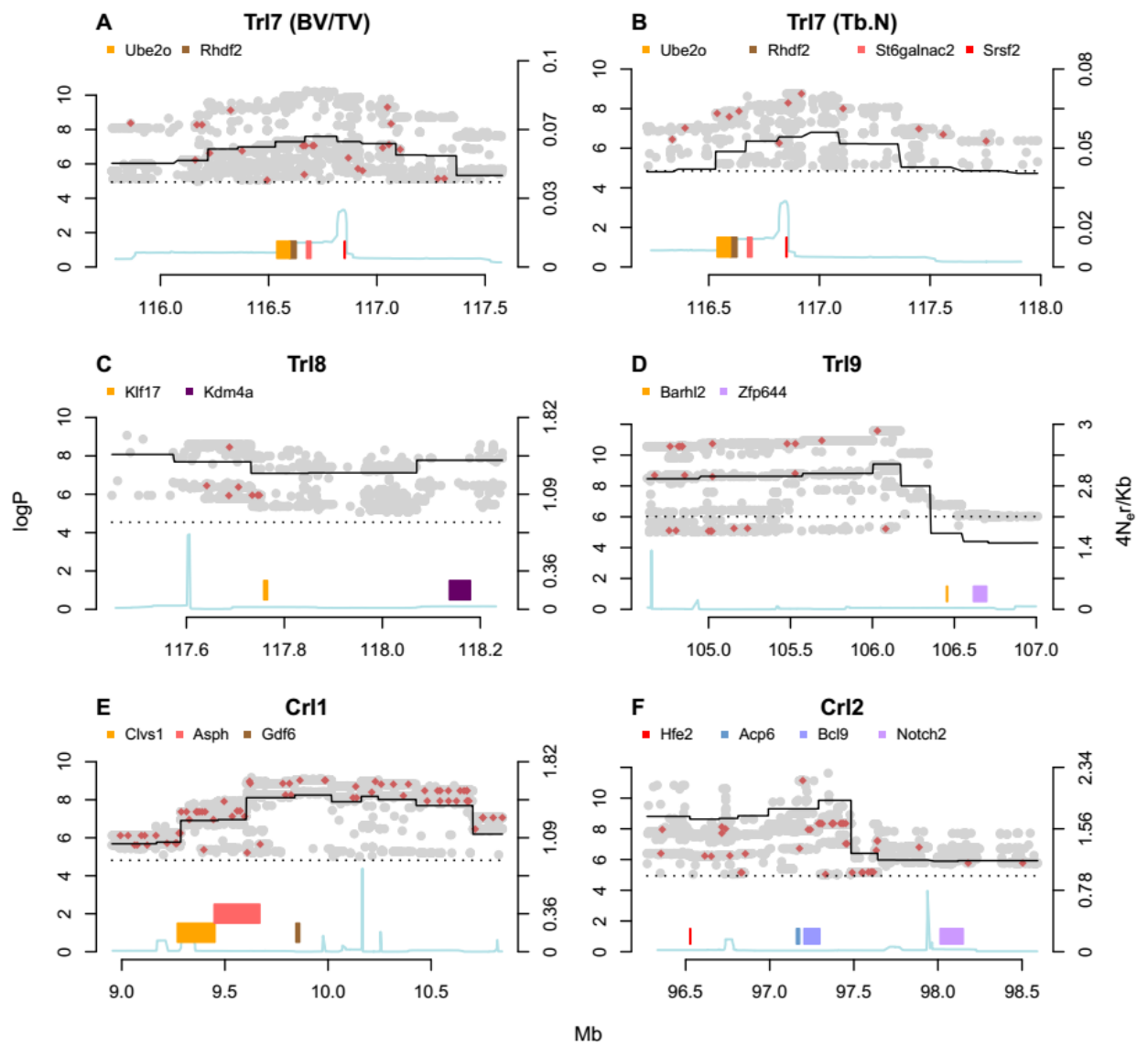


Figure 7

Levy_Fig7

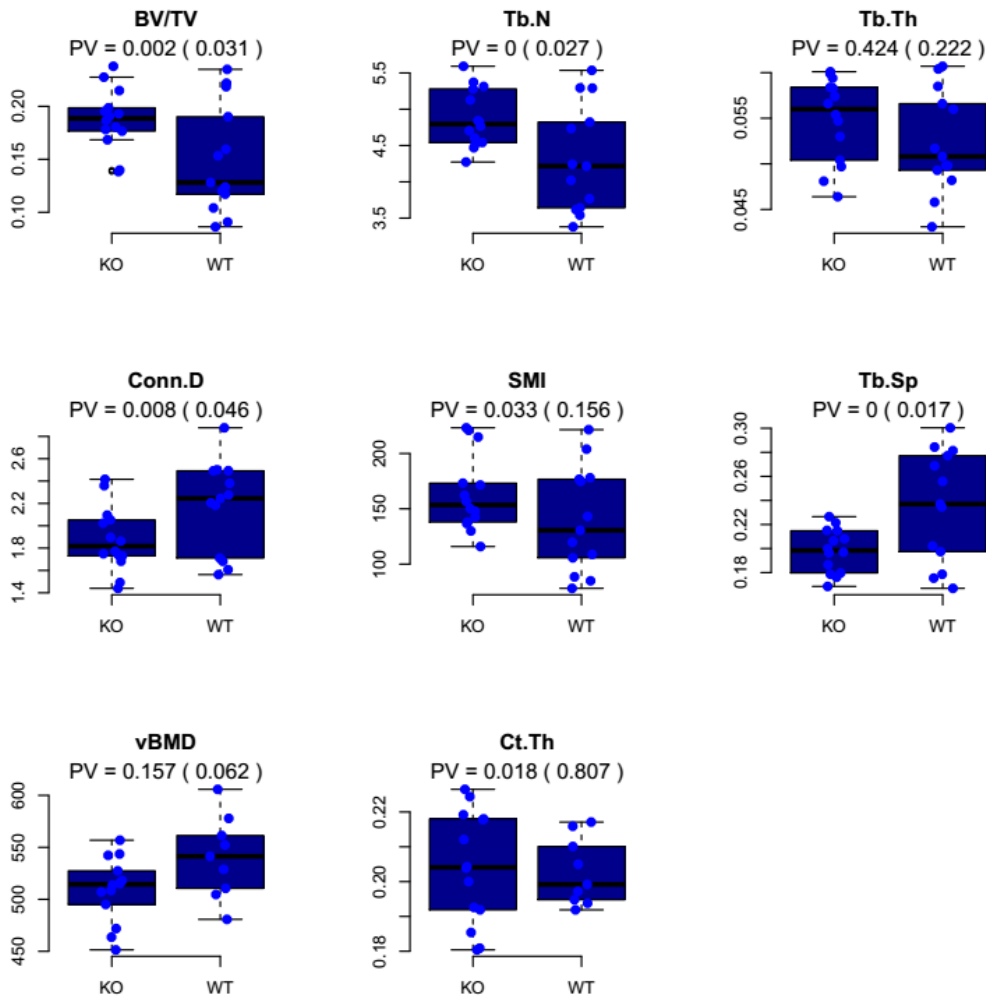


Figure 8

Levy_Fig8

